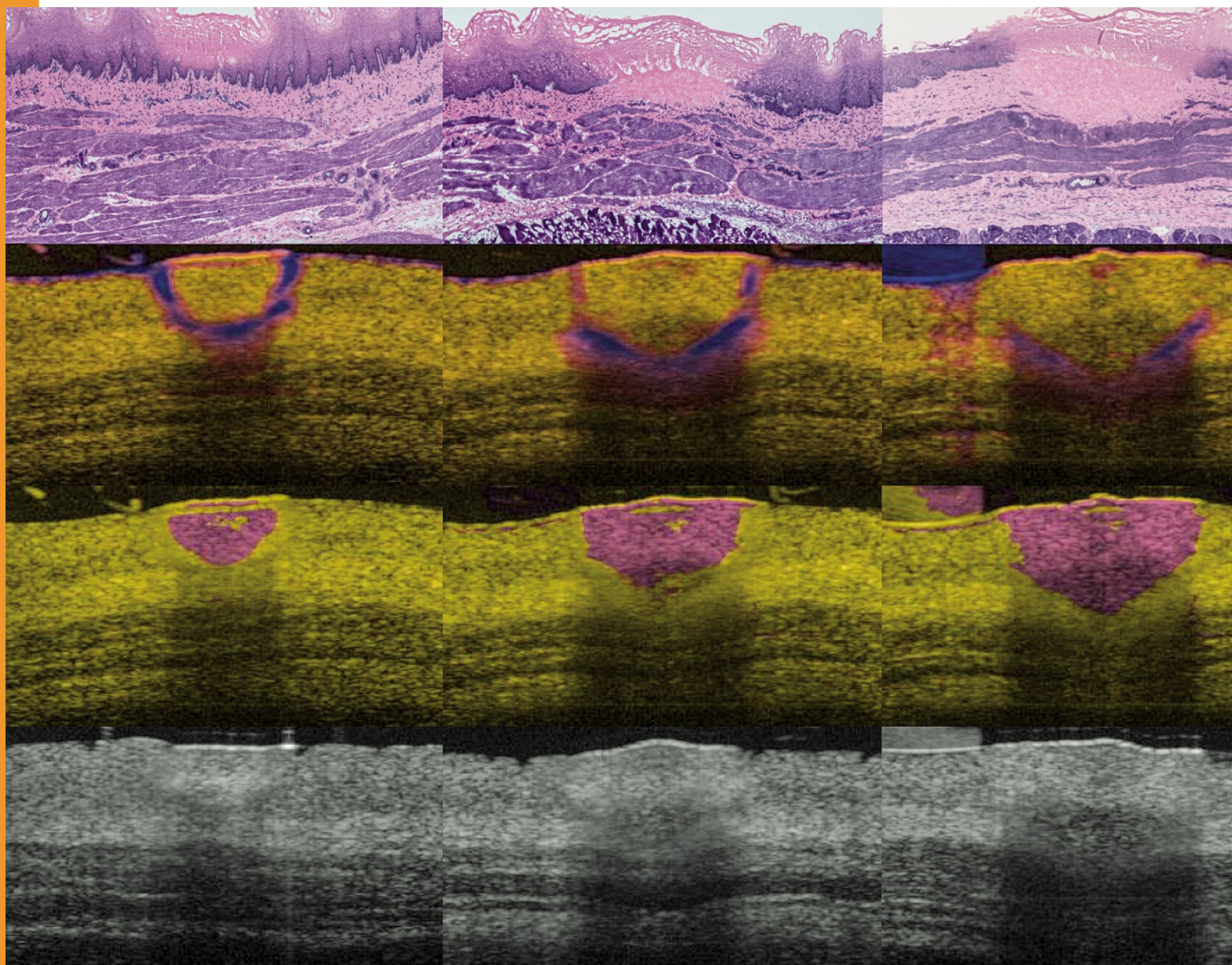


Journal of

1/17

BIOPHOTONICS

www.biophotonics-journal.org



Laser thermal therapy monitoring using complex differential variance in optical coherence tomography
W. C. Y. Lo, N. Uribe-Patarroyo, A. S. Nam, M. Villiger,
B. J. Vakoc, B. E. Bouma

WILEY-VCH

FULL ARTICLE

Laser thermal therapy monitoring using complex differential variance in optical coherence tomography

William C. Y. Lo*,^{1,2}, Néstor Uribe-Patarroyo¹, Ahhyun S. Nam^{1,3}, Martin Villiger¹, Benjamin J. Vakoc^{1,2}, and Brett E. Bouma^{1,2}

¹ Wellman Center for Photomedicine and Department of Dermatology, Massachusetts General Hospital and Harvard Medical School, 40 Blossom Street, Boston, Massachusetts 02114, USA

² Harvard-Massachusetts Institute of Technology Division of Health Sciences and Technology, Cambridge, Massachusetts 02142, USA

³ Department of Mechanical Engineering, Massachusetts Institute of Technology, 77 Massachusetts Avenue, Cambridge, Massachusetts 02139, USA

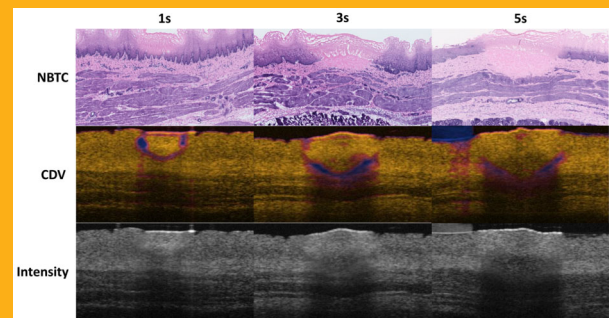
Received 27 March 2016, revised 10 July 2016, accepted 21 August 2016

Published online 13 September 2016

Key words: laser thermal therapy, optical coherence tomography, retina, skin, esophagus

Conventional thermal therapy monitoring techniques based on temperature are often invasive, limited by point sampling, and are indirect measures of tissue injury, while techniques such as magnetic resonance and ultrasound thermometry are limited by their spatial resolution. The visualization of the thermal coagulation zone at high spatial resolution is particularly critical to the precise delivery of thermal energy to epithelial lesions. In this work, an integrated thulium laser thermal therapy monitoring system was developed based on complex differential variance (CDV), which enables the 2D visualization of the dynamics of the thermal coagulation process at high spatial and temporal resolution with an optical frequency domain imaging system. With proper calibration to correct for noise, the CDV-based technique was shown to accurately delineate the thermal coagulation zone, which is marked by the transition from high CDV upon heating to a significantly reduced CDV once the tissue is coagulated, in 3 different tissue types *ex vivo*: skin, retina, and esophagus.

The ability to delineate thermal lesions in multiple tissue types at high resolution opens up the possibility of performing microscopic image-guided procedures in a vast array of epithelial applications ranging from dermatology, ophthalmology, to gastroenterology and beyond.



1. Introduction

The current state-of-the-art techniques for clinical thermal therapy monitoring typically involve the use of temperature as part of the treatment feedback loop. Unfortunately, temperature measurements using thermocouples only permit point sampling, while emerging magnetic resonance thermometry techniques [1, 2] and ¹⁵O-water PET imaging [3] offer low spatiotemporal resolution and are expensive to use.

More recently, photoacoustic thermography of tissue was also investigated for the assessment of myocardial ablation lesions [4]. However, these temperature-based monitoring techniques can only provide an indirect estimate of tissue injury and the spatial resolution remains low for epithelial applications.

Within the domain of optical coherence tomography (OCT), several early studies explored the use of polarization-sensitive OCT (PS-OCT) for the assessment of thermal damage directly [5, 6]. In particular,

* Corresponding author: e-mail: Lo.William@mgh.harvard.edu

reduced tissue birefringence was observed with PS-OCT in thermally damaged porcine skin or tendon due to the denaturation of collagen, which is consistent with earlier studies in thermally damaged myocardium [7] and rat tail tendon [8] using polarizing light microscopy. PS-OCT was also shown to be useful for burn assessment in patients [9, 10] and for studying the remodeling of hypertrophic scars longitudinally *in vivo* [11]. In addition, catheter-based PS-OCT was demonstrated for radiofrequency ablation monitoring in porcine myocardium *ex vivo* [12], following earlier observation of changes in birefringence bands between untreated and ablated myocardial tissue with intensity-based OCT [14–16]. Recently, depolarization (in addition to linear retardance) was investigated to visualize radiofrequency-ablated myocardial tissue *ex vivo* using Mueller matrix polarimetry in a backscattered geometry [16]. However, these techniques are typically limited to tissue with high birefringence at baseline (e.g., muscle, skin, or tendon) and their broad application to real-time monitoring of thermal therapy in diverse tissue types remains challenging. As an alternative approach, we previously demonstrated the feasibility of visualizing injury depth in laser thermal therapy of porcine esophagus based on phase variations in OCT; however, this requires careful phase calibration or a highly phase-stable OCT system and was demonstrated in an M-mode imaging configuration, enabling only 1-D, single-point monitoring without structural information [17].

In the present work, we developed a 2-D thermal therapy monitoring algorithm (with potential extension to 3-D) using complex differential variance [18], which exploits the phase and intensity fluctuations during thermal therapy but does not require a highly phase-stable OCT system. The algorithm is applied

to the OCT data directly, so visualization of structural information simultaneously during therapy monitoring is not inhibited. To assess the feasibility of this approach for monitoring laser thermal therapy, a wavelength tunable thulium fiber laser (1860–1895 nm) was used, which takes advantage of a strong water absorption peak for thermal coagulation in biological tissue. Using the integrated thulium laser and OCT imaging setup, we demonstrate the ability of the CDV-based technique to accurately delineate the thermal coagulation boundary in 3 different tissue types: retina, skin, and esophagus, which opens up the possibility of performing *microscopic* image-guided interventions at high spatiotemporal resolution in numerous clinical applications.

2. Materials and methods

2.1 Laser thermal therapy experimental setup

Figure 1 shows the experimental setup used for the laser thermal therapy study. A detailed description of the optical frequency domain imaging system was reported previously [19]. Briefly, the system features a fiber ring wavelength-swept laser operating at 240 kHz with 4-fold interleaving, a center wavelength of 1310 nm and a 125 nm sweep range. An acousto-optic modulator was used in the reference arm to remove depth-degeneracy [20]. An imaging window of 10 mm, consisting of 1024 A-lines/B-scan, was scanned with a focused beam resulting in a $1/e^2$ radius of 32 μm of the lateral point spread function in the squared norm of the complex-valued tomogram.

A wavelength tunable thulium fiber laser (IPG Photonics, Oxford, MA), which provides single-

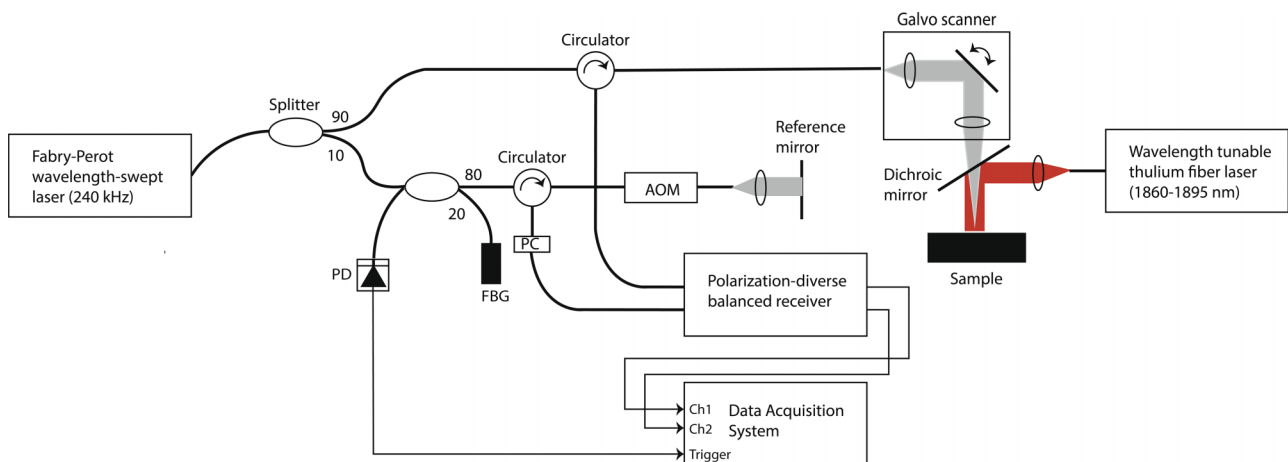


Figure 1 Schematics of the laser thermal therapy monitoring setup integrating an optical frequency domain imaging system with a wavelength tunable thulium fiber laser. Simultaneous OCT imaging and laser therapy with a thulium fiber laser is achieved using a dichroic mirror and programmable shutter to synchronize the timing of therapy. AOM, acousto-optic modulator; PC, polarization controller; PD, photodiode; FBG, fiber Bragg grating.

mode output from 1860 nm to 1895 nm, was used for laser thermal therapy. The benchtop setup integrated the thulium laser into the OCT optical path using a dichroic mirror. The collimated beam with a $1/e^2$ diameter of $\sim 800 \mu\text{m}$, measured with the WinCamD UCD12 beam profiler (DataRay, Redding, CA), was aligned to the center of the imaging plane on the tissue surface and the wavelength was set to 1890 nm to match the water absorption peak. Output power was varied from 300 mW to 500 mW (60 W/cm^2 to 100 W/cm^2) to investigate the technique at various fluence rates, including those reaching tissue vaporization threshold [21].

2.2 Processing algorithm

Figure 2 provides an overview of the processing algorithm developed for laser thermal therapy monitoring and coagulation zone visualization in this study. We employed complex differential variance (CDV) [18], which exploits both intensity and phase variations, to map the dynamic fluctuations in the complex OCT signal during the thermal coagulation process and extended this implementation to calibrate for noise and to enable the intuitive visualization of the coagulation zone. For a pair of A-lines acquired at times t and $t+1$ (in M consecutive B-scans), CDV is computed as follows:

where $R(z, t)$ is the complex OCT signal, $R^*(z, t)$ its complex conjugate, $w(k)$ is a depth window function with length $2L+1$, and M indicates the number of consecutive B-scans used for averaging. Here, a Hanning window with a length of 11 ($L=5$) depth pixels was used and M was set to 10 B-scans (which results in an effective frame rate of 23 fps with 1024 A-lines/B-scan at a 240 kHz A-line rate). While this algorithm intrinsically rejects phase noise induced by small axial bulk tissue motion and synchronization errors, we observed an SNR-dependent increase in CDV in static regions resulting in a non-zero baseline CDV in deeper regions due to decreased SNR. Hence, we performed an SNR-dependent calibration of the CDV using a static region within the tissue next to the therapy zone (calibration window size: 20×10 pixels after down-sampling by $10\times$ in both the intensity image and raw CDV image, each with an original size of 1024×1024 pixels). The SNR-dependent CDV was fitted to an exponential decay and subtracted from the raw CDV to derive the calibrated CDV values (CDV_{cal}). The calibrated CDV was mapped onto the intensity OCT images for simultaneous visualization of underlying structures. Finally, the coagulation zone was visualized by highlighting regions that have reached a cumulative CDV threshold ξ and returned to a low CDV below ϵ upon coagulation, where the cumulative CDV as a function of time t

$$f_{\text{CDV}}(z) = \sqrt{1 - \frac{\sum_{t=0}^{M-1} \left| \sum_{l=-L}^L w(l) R(z-l, t) R^*(z-l, t+1) \right|}{\sum_{t=0}^{M-1} \sum_{l=-L}^L w(l) \frac{1}{2} [|R(z-l, t)|^2 + |R(z-l, t+1)|^2]}} \quad (1)$$

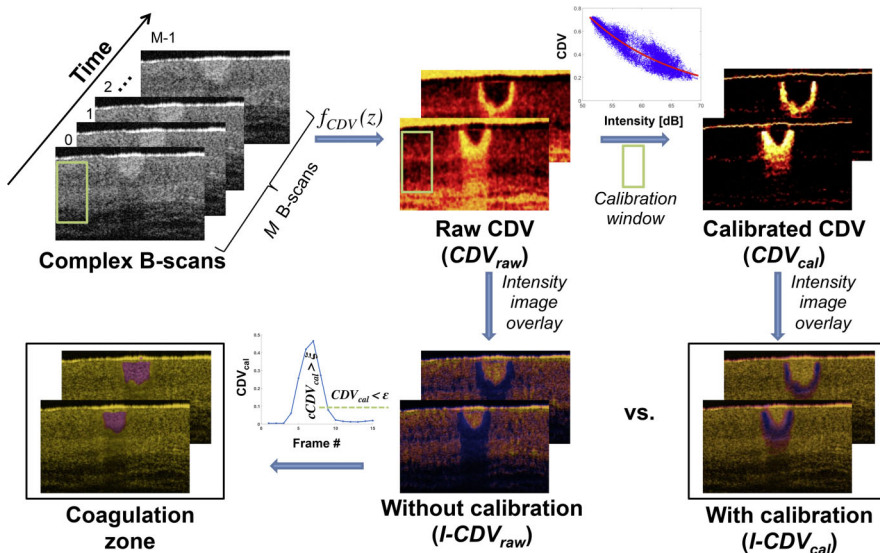


Figure 2 Overview of processing algorithm for laser thermal therapy monitoring and coagulation zone visualization. Complex B-scans are processed in batches of M B-scans to produce raw CDV (CDV_{raw}) frames. Using a calibration window in a static region within the tissue, a calibration curve for the SNR dependence is estimated and applied to produce the calibrated CDV frames (CDV_{cal}). The final image is produced by overlaying the intensity image on top ($I\text{-CDV}_{\text{raw}}$ vs. $I\text{-CDV}_{\text{cal}}$), showing significant improvements with calibration. The coagulation zone is visualized by detecting regions that have reached the cumulative CDV threshold (ξ) and returned to a low instantaneous CDV upon coagulation (ϵ).

is defined as

$$cCDV_{cal}(t) = \sum_{\tau=0}^t CDV_{cal}(\tau) \quad (2)$$

and the coagulation zone $c(t)$, which is a binary mask that evolves as a function of time t , is determined as follows:

$$c(t) = \{cCDV_{cal}(t) > \xi\} \cap \{CDV_{cal}(t) < \varepsilon\} \quad (3)$$

2.3 Histological analysis

Tissue samples (bovine eye, porcine skin, and porcine esophagus) were harvested immediately after sacrifice and laser thermal therapy was performed *ex vivo* at room temperature. Tissue marking dyes were placed on each side of the laser therapy spot for co-registration of OCT images with histology. Tissue samples were trimmed and sectioned for either routine H&E histology or nitroblue tetrazolium chloride (NBTC) histology (with eosin counterstain) after embedding in optimum cutting temperature compound for frozen sections at 10 μm . NBTC stains for the activity of NADH-diaphorase, which subsides upon thermal coagulation and cell death [22].

3. Results

Figure 3 shows an example of monitoring laser therapy in bovine retina *ex vivo* using the CDV-based approach, demonstrating the ability to clearly visualize the dynamics of the laser-induced heating and coagulation process. The center therapy zone exhibits a rapid rise in CDV (purple) extending from the retina into the sclera upon the initiation of laser therapy at 300 mW (60 W/cm²). A growing zone with reduced CDV (yellow), surrounded by a rim of high CDV (purple/red), was observed as the process continued. This growing zone (marked by the blue dotted lines on each image) corresponds well histologically to the thermal coagulation zone marked by the denaturation of the collagen in the fibrous sclera layer in H&E.

Figure 4 shows a similar thermal coagulation signature in the rapidly expanding zone with reduced CDV surrounded by high CDV for the case of porcine skin *ex vivo* at the same power setting of 300 mW (60 W/cm²). The panel clearly reveals the early dynamics of the coagulation process for the first 1.5 s. Lesion formation appeared slightly faster in this case compared to the retina, most likely due to differences in tissue properties and the presence

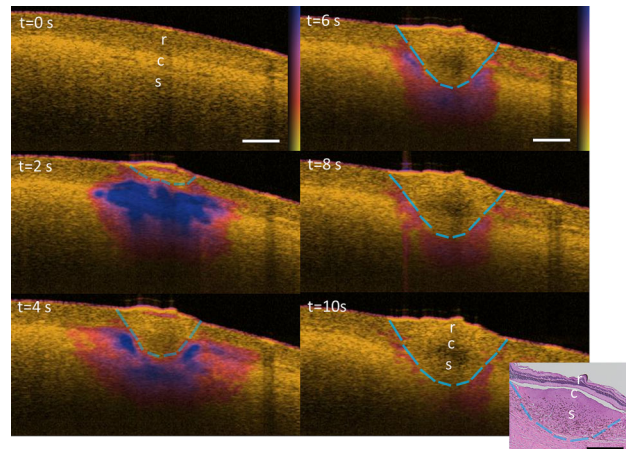


Figure 3 Laser thermal therapy monitoring in bovine retina *ex vivo* using calibrated complex differential variance (CDV_{cal}). Images represent cross-sectional slices at the center of the thulium laser therapy beam (300 mW or 60 W/cm²) every 2 s for 10 s, where CDV_{cal} was overlaid on intensity images. H&E histology (inset) reveals a coagulation zone extending into the sclera that corresponds with the region with reduced CDV (yellow) at the center delineated by an expanding boundary with high CDV (purple). Colorbar (CDV_{cal}) ranges from 0 to 0.5. Blue dotted lines, coagulation zone. r, retina; c, choroid; s, sclera. Scale bars = 500 μm .

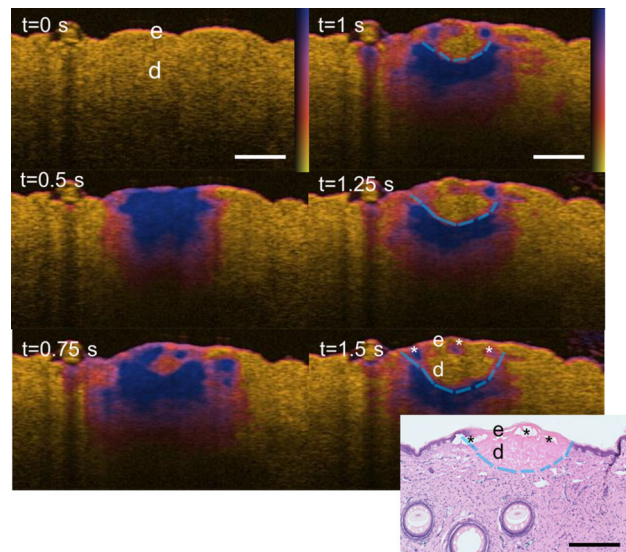


Figure 4 Laser therapy monitoring in porcine skin *ex vivo* at 300 mW (60 W/cm²) for 1.5 s. NBTC histology with eosin counterstaining (inset) at treatment endpoint confirms that the extent and shape of thermal damage in the dermis (NBTC-negative region in pink) corresponds well with the expanding zone with reduced CDV (yellow) delineated by a boundary with high CDV (purple). Colorbar (CDV_{cal}) ranges from 0 to 0.5. Blue dotted lines, coagulation zone. e, epidermis; d, dermis. Asterisks (*), air bubbles. Scale bars = 500 μm .

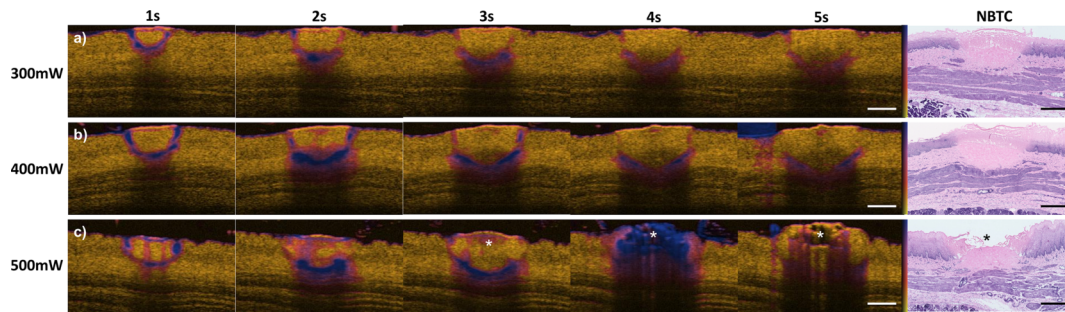


Figure 5 Effect of increasing the output power of the thulium fiber laser during laser therapy in porcine esophagus *ex vivo*: (a) 300 mW [60 W/cm²], (b) 400 mW [80 W/cm²] (Supplementary Video 1), and (c) 500 mW [100 W/cm²]. NBTC histology with counterstaining was performed at the treatment endpoint ($t = 5$ s), showing close correspondence between the NBTC-negative region (pink) and the zone with reduced CDV (yellow) delineated by a boundary with high CDV (purple). Color-bar (CDV_{cal}) ranges from 0 to 0.5. Asterisks (*), air bubbles. Scale bars = 500 μ m.

of a small layer of vitreous humor on top of the retina which absorbed part of the thermal energy delivered. NBTC histology was performed to confirm the boundary of thermal coagulation, and the NBTC-negative region, indicative of thermal damage, corresponds well with the coagulation zone indicated by the CDV-based technique.

To further investigate this approach for delineating lesion boundaries in different tissue types and at different laser power settings, we performed another experiment in porcine esophagus *ex vivo* using laser power from 300 mW to 500 mW, corresponding to fluence rates of 60 W/cm² to 100 W/cm² (Figure 5). The lesion boundary was particularly well defined at the early phase ($t = 1$ – 3 s), but became less clear as the thermal coagulation zone expanded, especially at the lowest fluence rate (60 W/cm²). Interestingly, at the highest fluence rate tested (100 W/cm²), a superficial layer with increased CDV was observed inside the therapy zone due to the formation of expanding air bubbles that eventually burst with tissue vaporization (at $t = 4$ s when the instantaneous CDV reached the maximum value) as confirmed by histology.

To better visualize the evolution of the coagulation zone over time, the history of CDV values was used to detect regions that have reached the coagulation threshold as defined in Eq. (3), highlighted in purple and overlaid onto the intensity images (Figure 6). This visualization technique overcomes the limitation of displaying the instantaneous CDV, when the boundary becomes less visible with the expansion of the coagulation zone, especially at the lower power settings. Even at the highest power setting tested (when the tissue vaporization threshold was reached), this approach still provided a good estimate of the coagulation zone, as confirmed by NBTC histology.

Finally, histological validation with NBTC staining was performed at representative time points during laser therapy from 1 s to 5 s at 400 mW (80 W/cm²), showing that the coagulation zone delineated by the CDV approach corresponds well histologically to the NBTC-negative region and thermal damage (Figure 7). In particular, at the early phase of therapy ($t = 1$ s), the CDV-based technique indicates an injury depth limited to the epithelium (reaching the lamina propria at $t = 3$ s) while at the treatment

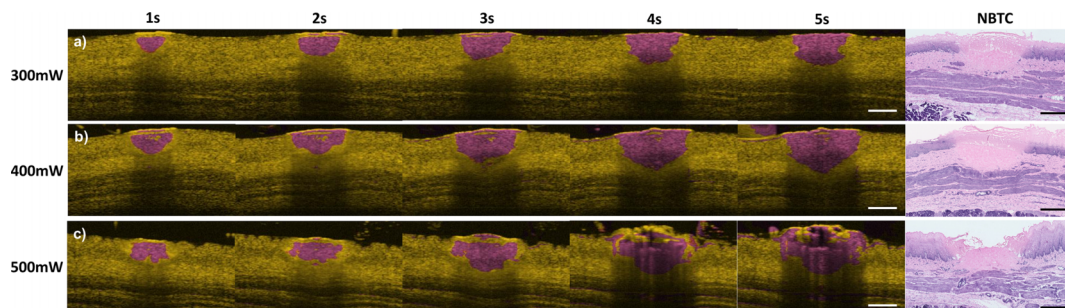


Figure 6 Visualization of the coagulation zone in porcine esophagus using the history of CDV values at different power settings: (a) 300 mW [60 W/cm²], (b) 400 mW [80 W/cm²] (Supplementary Video 1), and (c) 500 mW [100 W/cm²]. Purple color indicates regions that have reached the coagulation threshold defined by the cumulative CDV parameter and low instantaneous CDV ($\xi = 2$ and $\varepsilon = 0.1$), which provides an alternative way to more clearly delineate the thermal coagulation zone as confirmed by NBTC histology. Scale bars = 500 μ m.

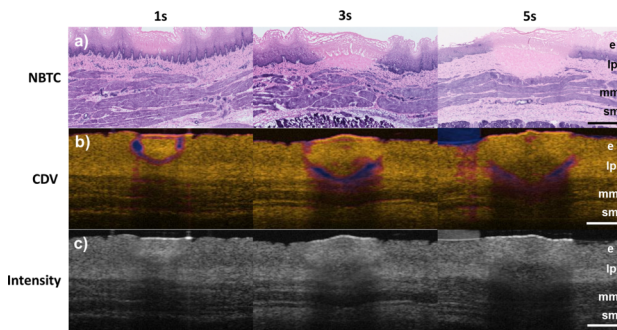


Figure 7 Histological validation of CDV-based coagulation zone monitoring in porcine esophagus *ex vivo* at 400 mW (80 W/cm²) for 5 s. NBTC histology with counterstaining was obtained at each representative time point (1 s, 3 s, and 5 s), showing close correspondence between the NBTC-negative coagulation zone (pink) (a) and the region showing the transition from high to low CDV (purple to yellow) (b), which is difficult to delineate clearly using intensity images alone (c). e, epithelium; lp, lamina propria; mm, muscularis mucosa; sm, submucosa. Scale bars = 500 μm.

endpoint ($t = 5$ s), the injury depth has reached the muscularis mucosa, as confirmed histologically by NBTC staining. By contrast, the lesion boundary is difficult to delineate with the intensity OCT images alone despite the increased backscattering observed in the coagulated tissue, especially as the shadow below the coagulated zone expanded at later time points (Figure 7c).

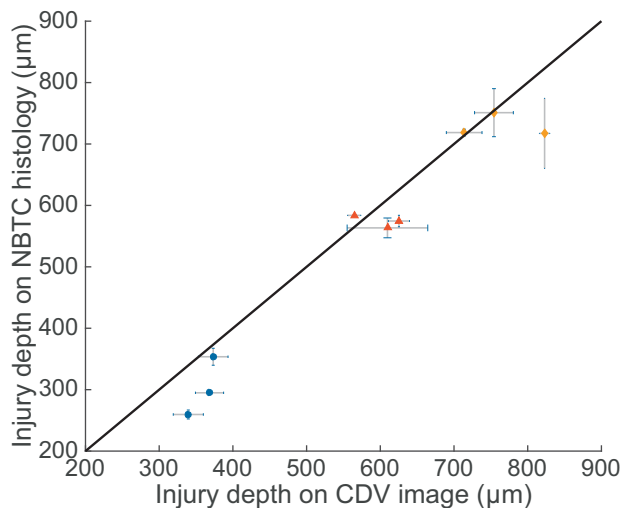


Figure 8 Quantitative validation of coagulation zone depth (injury depth) in porcine esophagus after laser therapy at 400 mW (80 W/cm²) for 1 s, 3 s, and 5 s. Each data point represents the mean \pm SD of the injury depths on the OCT (CDV) image and corresponding NBTC histology measured independently by three experts. The solid line represents perfect correlation of OCT and histology measurements for comparison. Blue circles, 400 mW (80 W/cm²) at 1 s. Red triangles, 400 mW (80 W/cm²) at 3 s. Yellow diamonds, 400 mW (80 W/cm²) at 5 s.

To further validate the findings systematically and quantitatively, three lesions were created for each therapy duration, and the depth of the coagulation zone (injury depth) was measured on corresponding CDV images and NBTC histology independently by three experts, showing good agreement between the CDV-based and NBTC-based measurements overall ($r^2 = 0.95$) (Figure 8). In cases where discrepancies were observed, the depth measured on NBTC histology was typically smaller than that measured using the CDV image (~50–100 μm), most likely due to variability in tissue shrinkage during frozen section processing as well as instantaneous thermal expansion and bubble formation in the superficial layer during therapy.

4. Discussion

In this study, we demonstrated the use of dynamic OCT measurements based on complex differential variance to accurately delineate the coagulation zone in laser thermal therapy and validated this approach histologically in 3 different tissue types: skin, retina, and esophagus. By overlaying this information directly on intensity OCT images, the active treatment zone was visualized simultaneously with the underlying tissue architecture, which enables lesions to be targeted more precisely. Compared to previous work based on PS-OCT or polarimetry-based techniques [5, 6, 12, 13], the current method is not limited to biological tissues with high birefringence at baseline (e.g. skin, muscle, and tendon) and has broader implications in a number of clinical applications.

However, there are several limitations to the current CDV-based approach. First, unlike PS-OCT where the thermal lesion can be readily imaged and visualized post treatment due to the loss of tissue birefringence, the CDV-based approach derives contrast from the real-time variations in phase and intensity signals that subside once the therapy beam is turned off. The need for real-time tracking also means that motion can lead to an artificial increase in CDV, which can be mitigated with increased imaging speed or similarly by decreasing the number of B-scans (M) used to compute CDV in Eq. (1), as well as various motion correction techniques [23–25]. Similarly, perfusion in living tissue can contribute to the CDV signal, but considering the time scale, the relative contribution will likely be smaller than the therapy-induced CDV signal. In addition, the active treatment zone boundary can become more difficult to delineate as the coagulation zone grows bigger and the CDV signal degrades as a function of depth. When the uncalibrated CDV values begin to saturate at depths approaching the noise floor (typically at a depth >1 – 1.5 mm), the dy-

namics of the heating process becomes increasingly difficult to observe, especially at lower fluence rates. Therefore, we have performed an SNR-dependent calibration to enable more robust visualization at greater depths, which provides an accurate estimate of the lesion boundary at the different depths tested. However, the depth limitation is also a fundamental limitation of OCT imaging, which is difficult to overcome even with calibration for noise, due to inherent limits on system sensitivity and penetration depth of light. To further improve the visualization of the coagulation zone, we developed an alternative visualization method in which the history of CDV values is tracked and regions that have reached a cumulative CDV threshold ξ and returned to an instantaneous CDV below ε as defined in Eq. (3) are highlighted. While the coagulation threshold is likely different between tissue types, this visualization strategy provides a good estimate of the growing coagulation zone that would be more difficult to appreciate with the instantaneous CDV alone.

Compared to our earlier work on monitoring laser therapy with phase variations in M-mode imaging [17], the current CDV-based approach was developed to overcome small axial bulk motion and phase jitter from data acquisition synchronization through the use of a depth window as defined in Eq. (1), which eliminates the need for a highly phase-stable OCT system or precise phase calibration [21]. We further demonstrated 2-D, cross-sectional therapy monitoring in different tissue types (with potential extension to 3-D) to enable simultaneous visualization of underlying tissue structures. It is interesting to observe in both our earlier study and the current study that the active treatment zone is marked by increased phase variation or CDV and the growing coagulation zone corresponds very well to the region where the phase variation or CDV has subsided.

By providing real-time therapy monitoring using the CDV-based technique, more targeted and personalized thermal therapy delivery can be achieved in dermatology, ophthalmology, gastroenterology, and beyond. An interesting opportunity provided by this promising therapy monitoring approach is the ability to precisely control various laser parameters, such as power, wavelength, and duration of therapy, to better tailor the therapy to the target lesion with immediate feedback [20]. For example, the current technology can be applied to tailor the laser treatment of hypertrophic scars [26], laser photocoagulation in diabetic retinopathy especially in the sub-threshold regime [27], and more targeted thermal therapy of epithelial lesions such as Barrett's esophagus with high-grade dysplasia [17, 20, 25]. Using the current approach, more precise thermal therapy in epithelial lesions may be achieved by tailoring the thermal injury to the desired depth; for example, in the treatment of Barrett's esophagus, it is important

to avoid excessive damage beyond the submucosa to reduce the risk of stricture formation [29]. The ability to delineate thermal lesions in different tissue types, at high spatiotemporal resolution, opens up the possibility of performing *microscopic* image-guided procedures in a vast array of epithelial applications in the future.

Supporting Information

Additional supporting information may be found in the online version of this article at the publisher's website.

Supplementary Video 1: Laser thermal therapy monitoring in porcine esophagus *ex vivo* using complex differential variance (400 mW or 80 W/cm² for 5 s).

Acknowledgements Research reported in this publication was funded in part by the National Institutes of Health P41 EB015903 grant. WCYL was supported by the Canadian Institutes of Health Research (CIHR) Doctoral Foreign Study Award.

Author Biographies Please see Supporting Information online.

References

- [1] O. Seror, M. Lepetit-Coiffé, B. Le Bail, B. D. de Senneville, H. Trillaud, C. Moonen, and B. Quesson, *Eur. Radiol.* **18**(2), 408–16 (2008).
- [2] B. D. de Senneville, C. Mougenot, B. Quesson, I. Dragonu, N. Grenier, and C. T. W. Moonen, *Eur. Radiol.* **17**(9), 2401–2410 (2007).
- [3] A. Bao, B. Goins, G. D. Dodd, A. Soundararajan, C. Santoyo, R. A. Otto, M. D. Davis, and W. T. Phillips, *J. Nucl. Med.* **49**(10), 1723–1729 (2008).
- [4] H. Ke, S. Tai, and L. V. Wang, *J. Biomed. Opt.*, **19**(2), 26003 (2014).
- [5] J. De Boer, S. Srinivas, A. Malekafzali, Z. Chen, and J. Nelson, *Opt. Express* **3**(6), 212–218 (1998).
- [6] K. Schoenenberger, B. W. Colston, D. J. Maitland, L. B. Da Silva, and M. J. Everett, *Appl. Opt.* **37**(25), 6026 (1998).
- [7] S. Thomsen, J. A. Pearce, and W. F. Cheong, *IEEE Trans. Biomed. Eng.* **36**(12), 1174–1179 (1989).
- [8] D. J. Maitland and J. T. Walsh, *Lasers Surg. Med.* **20**(3), 310–318 (1997).
- [9] M. C. Pierce, R. L. Sheridan, B. Hyle Park, B. Cense, and J. F. De Boer, *Burns* **30**(6), 511–517 (2004).
- [10] K. H. Kim, M. C. Pierce, G. Maguluri, B. H. Park, M. Lydon, and J. F. De Boer, *J. Biomed. Opt.* **17**(6), 066012 (2012).
- [11] W. C. Y. Lo, M. Villiger, A. Golberg, G. F. Broelsch, S. Khan, C. G. Lian, W. G. Austen Jr., M. Yarmush,

- and B. E. Bouma, *J. Invest. Dermatol.* **136**(1), 84–92 (2016).
- [12] X. Fu, Z. Wang, H. Wang, Y. T. Wang, M. W. Jenkins, and A. M. Rollins, *Opt. Lett.* **39**(17), 5066–5069 (2014).
- [13] C. P. Fleming, K. J. Quan, and A. M. Rollins, *J. Biomed. Opt.* **15**(4), 041510 (2013).
- [14] C. P. Fleming, H. Wang, K. J. Quan, and A. M. Rollins, *J. Biomed. Opt.* **15**(3), 030516 (2013).
- [15] C. P. Fleming, K. J. Quan, H. Wang, G. Amit, and A. M. Rollins, *Opt. Express* **18**(3), 3079–3092 (2010).
- [16] I. Ahmad, A. Gribble, M. Ikram, M. Pop, and A. Vitkin, *J. Biophotonics* **10**, 1–10 (2015).
- [17] B. J. Vakoc, G. J. Tearney, and B. E. Bouma, *J. Biomed. Opt.* **12**(2), 020501 (2007).
- [18] A. S. Nam, I. Chico-Calero, B. J. Vakoc, *Biomed. Opt. Express* **5**(11), 3822–3832 (2014).
- [19] C. Jun, M. Villiger, W. Y. Oh, and B. E. Bouma, *Opt. Express* **22**(21), 2919–2921 (2014).
- [20] S. Yun, G. Tearney, J. de Boer, and B. Bouma, *Opt. Express* **12**(20), 4822–4828 (2004).
- [21] M. Villiger, A. Soroka, G. J. Tearney, B. E. Bouma, and B. J. Vakoc, *J. Biomed. Opt.* **16**(11), 118001–118001 (2011).
- [22] R. A. Neumann, R. M. Knobler, F. Pieczkowski, and W. Gebhart, *J. Am. Acad. Dermatol.* **25**(6), 991–998 (1991).
- [23] N. D. Shemonski, S. S. Ahn, Y.-Z. Liu, F. A. South, P. S. Carney, and S. A. Boppart, *Biomed. Opt. Express* **5**(12), 4131–43 (2014).
- [24] V. X. Yang, M. L. Gordon, A. Mok, Y. Zhao, Z. Chen, R. S. Cobbold, B. C. Wilson, and I. Alex Vitkin, *Optics Communications* **208**(4)–(6), 209–214 (2002).
- [25] L. An, H. M. Subhush, D. J. Wilson, and R. K. Wang, *J. Biomed. Opt.* **15**(2), 026011 (2010).
- [26] R. R. Anderson, M. B. Donelan, C. Hivnor, E. Greeson, E. V. Ross, P. R. Shumaker, N. S. Uebelhoer, and J. S. Waibel, *JAMA dermatology* **150**(2), 187–193 (2014).
- [27] P. Romero-Aroca, J. Reyes-Torres, M. Baget-Bernaldiz, and C. Blasco-Suñe, *Curr. Diabetes Rev.* **10**(2), 100–112 (2014).
- [28] K. K. Wang and R. E. Sampliner, *Am. J. Gastroenterol.* **103**(3), 788–797 (2008).
- [29] N. J. Shaheen and D. J. Frantz, *Curr. Opin. Gastroenterol.* **26**(4), 361–366 (2010).